Results in Engineering 17 (2023) 100992

Contents lists available at ScienceDirect

Results in Engineering

journal homepage: www.sciencedirect.com/journal/results-in-engineering

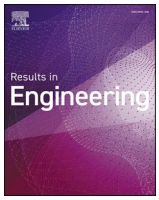

Novel design of a rotary calciner internally heated with electrical axial heaters: Experiments and modelling

Ron M. Jacob *, Lars-André Tokheim

University of South-Eastern Norway, Kjølnes Ring 56, 3918, Porsgrunn, Norway

ARTICLE INFO

Keywords:
Electrification
Rotary calciner
Internal heating
CO_2 emissions
Lime production

ABSTRACT

As the share of renewable energy increases, green electricity may help reduce the carbon footprint in the lime industry. Electrifying the calciner can produce relatively pure CO_2 from the calcination process ($CaCO_3 \rightarrow CaO + CO_2$), which may be utilized or stored. All the previous literature studied electrically heated rotary calciner with external heating. This work presents a novel design of an electrical rotary calciner through which internal heating is possible. The design can utilize existing kiln drums made from relatively inexpensive refractory and steel materials. The designed calciner operated smoothly for around four days, and the concept was technically feasible. The outer wall temperature and calcination degree was measured during the condition of a pseudo-steady state in the calciner. A model was developed and implemented in OpenModelica, which was validated by comparing it against measured variables. The modelling results revealed that the current setup had low thermal efficiency, as the heat loss amounted to around 60%, and the average heat transfer coefficient was around 101 W/(m^2K). A step-by-step procedure with the help of the model was discussed to improve heat efficiency and reduce heat loss by up to 11% by improving thermal insulation and increasing the residence time of particles. With the improved thermal efficiency, energy intensity and electricity cost per unit CO_2 were reduced from 35 to 7 MJ/kg-CO_2 and 4.9 to 1 NOK/kg-CO_2, respectively. So, improving thermal efficiency can improve both the environmental and economic aspect of the process.

1. Introduction

Renewable electricity production is steadily increasing [1], and green electricity could be an alternative to decarbonizing emission-intensive industries in the future. In lime production, the main reaction is calcite decomposition ($CaCO_3 \rightarrow CaO + CO_2$), and the process temperature is in the range 900–1200 °C. Depending on the calciner design, 3.2–9.2 MJ/kg-lime is consumed in the calciner, with an average of 4.25 MJ/kg-lime [2]. The average CO_2 emitted from the calcite decomposition is estimated to be around 0.75 kg-CO_2/kg-lime, whereas around 0.32 kg-CO_2/kg-lime is emitted from the fuel burning [2]. The CO_2 coming from calcite decomposition is clearly more significant and this amounts to 70% of the emissions. So, electrifying the calciner with green energy can cut fuel combustion emissions and produce high-purity CO_2 from calcite decomposition for direct capture.

Electrifying the calciner is also attractive for the cement industry as the contribution of CO_2 emission from calcite decomposition is very high in the cement industry. A previous mass and energy balance on the cement industry with an electrified calciner indicates that the emission could be reduced by up to 78% [3].

Another advantage of electrifying the calciner is that the contaminants from fuel ash will not be present in the final product, and a high-quality lime can be produced. Around 88% of the lime demand is of high quality with high reactivity [4]. So, the lime produced in an electrified calciner can cater to a large share of the demand.

Parallel flow regenerative kilns are used most widely in the EU lime industry mainly due to their energy efficiency [4,5]. An electrified version of this technology has not yet been demonstrated. Calix has developed an indirectly heated drop tube calciner, which is being tested at a pilot scale in the LEILAC (Low Emissions Intensity Lime and Cement) project [6]. The limestone is dropped in an externally heated tube in such a reactor. The heated external tube provides the energy for calcite decomposition. In the first phase, LIELAC used fuel burning as external heat. However, in the second phase, they also intend to test electrical heating [7].

Rotary calciners are also used for lime production [2]. Electrically heated rotary calciner are available in the market, but all the available calciners are externally heated. The previous studies on electrified rotary calciner were also done on systems with an externally heated rotary

* Corresponding author.Borgehaven 23, Porsgrunn, 3911, Norway.
E-mail addresses: Ron.Jacob@usn.no, ronmjacob1994@gmail.com (R.M. Jacob), Lars.A.Tokheim@usn.no (L.-A. Tokheim).

https://doi.org/10.1016/j.rineng.2023.100992
Received 5 December 2022; Received in revised form 15 February 2023; Accepted 27 February 2023
Available online 1 March 2023

Nomenclature

Small letters

$c_{p,a}$	Specific heat capacity of air, J/(kg·K)
$d_{d,i}$	Internal diameter of calciner drum, m
$d_{d,o}$	Outer diameter of calciner drum, m
d_e	Diameter of heating element, m
g	Gravitational acceleration, m/s^2
h_b	Average bed height, m
h_{cb}	Heat transfer coefficient in the covered bed, W/(m^{2}K)
h_L	Overall heat loss coefficient from outer drum, W/(m^{2}K)
$h_{L,C}$	Heat loss coefficient due to convection, W/(m^{2}K)
$h_{L,R}$	Heat loss coefficient due to radiation, W/(m^{2}K)
k_a	Thermal conductivity of air, W/(m·K)
k_b	Effective conductivity of bed material, W/(m·K)
k_C	Thermal conductivity of the produced lime, W/(m·K)
$k_{c,D}$	Kinetics of CO_2 diffusion through the lime (CaO) layer, mol/(m^2·s·Pa)
$k_{c,r}$	Kinetics of calcite decomposition, mol/(m^2·s·Pa)
k_d	Thermal conductivity of calciner drum, W/(m·K)
k_l	Thermal conductivity of limestone, W/(m·K)
l_d	Length of calciner drum, m
l_e	Length of heating element, m
$l_{e,b}$	Perpendicular length from element to bed, m
$\dot{m}$	Feeding rate of limestone, kg/s
m_b	Mass of accumulated bed material, m
n_e	Number of heating element inside calciner
$\dot{n}_i$	Molar flow rate of component i in the calciner, mol/s
$\dot{n}_{i,g}$	Molar generation of component i in the calciner, mol/s
p_a	Atmospheric pressure, Pa
p_{avg}	Average pressure of CO_2 diffusing through porous lime, Pa
p_{eq}	Equilibrium pressure for calcite decomposition, Pa
p_{CO2}	Partial pressure of CO_2 in the calciner, Pa
$p_{CO2,c}$	Partial pressure of CO_2 at the reacting calcite surface, Pa
$\dot{q}_b$	Total heat transferred to particle bed, W
$\dot{q}_{cb}$	Total heat transferred to the covered bed, W
$\dot{q}_d$	Radiative heat transferred to the inner drum, W
$\dot{q}_e$	Total heat generated in the heating elements, W
$\dot{q}_{eb}$	Total heat transferred to the exposed bed, W
$\dot{q}_L$	Total heat lost to the environment, W
r_c	Overall reaction rate of calcite decomposition, mol/s
r_{pore}	Pore radius in the produced lime from calcite decomposition, m
s_e	Spacing between the heating elements, m
t_d	Thickness of calciner drum, m
w_b	Width of bed, m
w_e	Width of element, m
x_C	Initial mass fraction of $CaCO_3$ in the limestone

Capital letters:

A_C	Surface area of each spherical calcite core, m^2
A_{cd}	Surface area of covered drum, m^2
$A_{d,o}$	Total surface area of outer drum, m^2
A_e	Surface area of all heating elements, m^2
A_{eb}	Surface area of exposed bed, m^2
A_{ed}	Surface area of exposed drum, m^2
A_{fac}	Area factor to account for excess area in reacting calcite from presence of pores,
D_{CO2}	Overall diffusivity of CO_2 through produced lime (CaO) layer, m^2/s
D_K	Knudsen diffusivity, m^2/s
D_M	Molecular diffusivity, m^2/s
$E_{b,b}$	Black body emission from the bed, W/m^2
$E_{b,d}$	Black body emission from the inner drum, W/m^2
$E_{b,e}$	Black body emission from heating elements, W/m^2
$E_{b,g}$	Black body emission from the gas, W/m^2
$F_{b,b}$	View factor from bed to bed
$F_{b,d}$	View factor from bed to drum
$F_{b,e}$	View factor from bed to element
$F_{b,g}$	View factor from bed to gas
$F_{d,b}$	View factor from drum to bed
$F_{d,e}$	View factor from drum to element
$F_{d,g}$	View factor from drum to gas
$F_{e,b}$	View factor from element to bed
$F_{e,d}$	View factor from element to drum
$F_{e,e}$	View factor from element to element
$F_{e,g}$	View factor from element to gas
$\dot{H}$	Total enthalpy of all the flowing particles in the calciner, W
H_i	Specific enthalpy of component i in the calciner, J/mol
H_{ref}	Reference enthalpy defined at 25 °C and 1 bar, J/mol
J_b	Radiosity from the bed, W/m^2
J_d	Radiosity from the inner drum, W/m^2
J_e	Radiosity from the heating elements, W/m^2
J_g	Radiosity from the gas, W/m^2
LOI	Loss on ignition, %
M_a	Molecular mass of air, kg/mol
M_{CO2}	Molecular mass of CO_2, kg/kmol
N	Rotational speed of the calciner, RPS
N_{rc}	Total number of reacting particles inside calciner
Nu_D	Nusselt number from drum
P_e	Total electrical power supplied to heating elements, W
Pr	Prandtl number
R	Universal gas constant, J/(mol·K)
R_1	Radiative heat transfer resistance from element emissivity, 1/m^2
R_2	Radiative heat transfer resistance from view factor between drum and element, 1/m^2
R_3	Radiative heat transfer resistance from view factor between element and gas, 1/m^2
R_4	Radiative heat transfer resistance from view factor between bed and element, 1/m^2
R_5	Radiative heat transfer resistance from calciner drum, 1/m^2
R_6	Radiative heat transfer resistance from view factor between drum and gas, 1/m^2
R_7	Radiative heat transfer resistance from view factor between drum and bed, 1/m^2
R_8	Radiative heat transfer resistance from the bed, 1/m^2
R_9	Radiative heat transfer resistance from view factor between bed and gas, 1/m^2
Ra_D	Rayleigh Number
R_C	Instantaneous calcite radius, m
$R_{C,o}$	Average initial calcite radius, m
$R_{d,i}$	Internal radius of calciner drum, m
T_a	Ambient temperature, K
T_b	Average temperature of the bed, K
T_C	Temperature at the calcite core, K
$T_{d,i}$	Inner drum temperature, K
$T_{d,o}$	Outer drum temperature, K
T_f	Temperature of fluid outside the calciner outer shell, K
T_g	Temperature of gas (CO_2) inside calciner, K

Greek letters

γ_i	Stoichiometric coefficient component i in calcination reaction,
γ	Angle of repose, radians
ω_o	Extra angle formed by flowing particles relative to the horizontal axis, radians

σ_{CO2}	Effective collision diameter of CO_2, Å	τ_p	Tortuosity factor,
ε_{CaO}	Void fraction of produced porous lime,	ρ_b	Bulk density of limestone bed, kg/m^3
$\varepsilon_{d,i}$	Emissivity of calciner inner drum,	ρ_l	Approximate density of limestone, kg/m^3
$\varepsilon_{d,o}$	Emissivity of calciner outer drum,	Γ	Angle subtended by the particle bed, radians
ε_e	Emissivity of heating elements,	α_b	Effective thermal diffusivity of the bed, m^2/s
ε_l	Emissivity of limestone,	ϑ_a	Kinematic viscosity of air, m^2/s
ε_g	Emissivity of gas (CO_2) inside calciner,	α_a	Thermal diffusivity of air, m^2/s
ω	Calciner inclination, radians	μ_a	Dynamic viscosity of air, Pa·s
ω_D	Collision integral,	β	Thermal expansion coefficient of air, 1/K
σ	Stefan-Boltzmann's constant, W/(m^{2}K^4)	ρ_a	Density of air, kg/m^3
η_e	Efficiency of conversion from electricity to heat,		

drum [8,9]. The rotating drum in a rotary calciner is generally under high mechanical and thermal stresses [10]. So, the choice of drum material is critical to ensure mechanical stability. A regular fuel-fired rotary calciner has an inner layer with refractory to minimize heat loss and an outer steel shell for structural support [10]. The electrified externally heated rotary calciner can not be made from these materials as the thermal conductivity of the refractory is relatively low. Special expensive materials that can withstand mechanical and thermal stresses are needed. So, the material costs may be very high.

Internal heating of the electrified rotary calciner can solve the problem with the choice of drum materials. This concept can use existing materials made from refractory and steel shells. Since the drum material can tolerate extreme temperatures due to the protective refractory layer, the maximum temperature in the electrified rotary kiln is limited by the temperatures of the internal heating element. The higher temperature of the heat source means that the heat transfer is higher inside the system due to a larger temperature gradient [11].

Internal heating of a rotary calciner is the novelty explored in this work. The article aims to introduce the novel design of an internally heated electrical rotary calciner and to demonstrate its operation through experiments and a model. A steady-state 1-D model of the calciner is developed and implemented in OpenModelica version 1.19.2. This model is first validated by experimental results and is then used to study and suggest improvements to the efficiency of the process. Finally, the advantages and disadvantages of this technology based on operational experience are explained.

2. Experimental method

2.1. Experimental setup

The experiments are done in a rotary calciner with internal heating elements, as shown in Fig. 1.

Three internal heating elements made from silicon carbide are placed inside the calciner. Two thermocouples, one at the calciner inlet and another one at the outlet, are also installed to measure the inner calciner temperature continuously. The calciner drum is a cylindrical steel shell protected on the inside by a spray-cast concrete layer. The drum has eight longitudinal lifters. These lifters work almost like internal baffles [12–14], which can promote heat transfer due a better mixing in the bed [15]. The limestone is fed into the calciner with a system developed by PEAL. The feeding system has a silo, screw conveyor, hopper, and vibrator. Limestone is stored in the silo and transported to the hopper with the screw conveyor. The screw conveyor is controlled to maintain a specified weight in the hopper. This limestone can then flow into the calciner after passing through the vibrator. The feeding rate of the limestone is controlled by adjusting the vibration frequency.

The dimensions and characteristics of the rotary calciner and heating element are shown in Table 1 and Table 2, respectively. The dimensions of the rotary calciner were given as this was originally a fuel-fired system that was retrofitted with internal heating elements in the current project. The heating element length was equal to the inner length of the rotary drum so that it fit into the calciner. The available heating element with this length had a diameter of 55 mm and a power rating of 34 kW. The calciner was designed to have a maximum power of 100 kW, so three heating elements were inserted. The heating elements were arranged in staggered triangular form with a distance greater than their

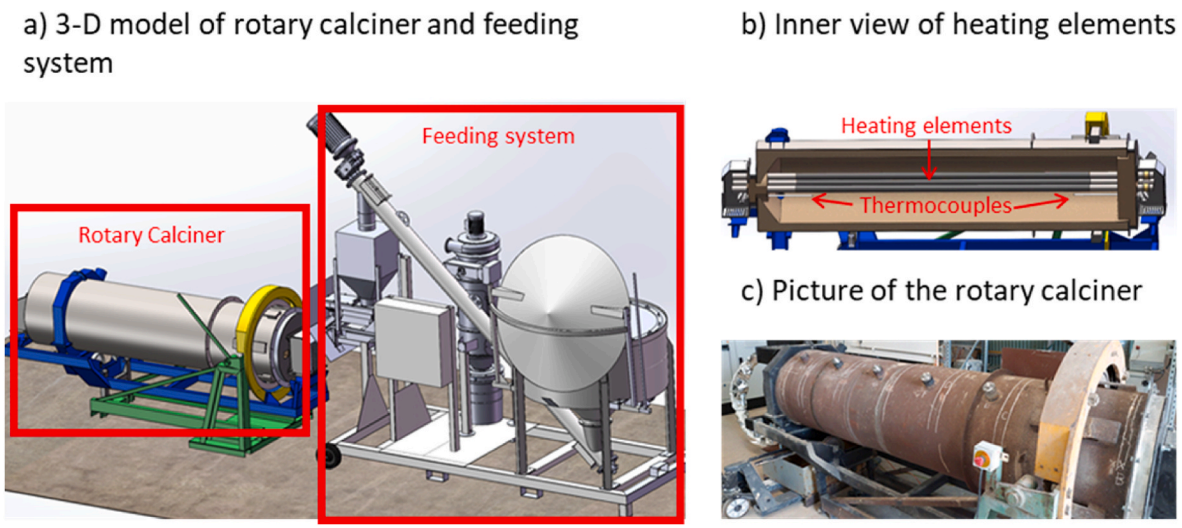

Fig. 1. Experimental setup.

Table 1
Dimensions and characteristics of the rotary calciner.

Parameters	Value	Remark
Internal diameter [m]	0.58	Measured
Internal length [m]	2.6	Measured
Effective thickness of the drum wall [m]	0.065	Measured
Lifter width [m]	0.1	Measured
Lifter height [m]	0.01	Measured
Effective conductivity of the drum wall [W/(m·K)]	1.2	Typical value of concrete [16]
Effective emissivity of the inner wall [−]	0.69	Typical value of limestone dust [17]
Effective emissivity of the outer wall [−]	0.88	Typical value of oxidized steel [16]

Table 2
Dimensions and characteristics of the heating elements.

Parameters	Value	Remark
Diameter [m]	0.055	Measured
Length [m]	2.6	Measured
Number of elements [−]	3	Measured
Space between heating elements [m]	0.075	Measured
Effective emissivity [−]	0.86	Typical value of silicon carbide [16]
Maximum power per heating element [kW]	34	Provided by the supplier (Kanthal)

diameter so that all three elements were visible from the particle bed.

2.2. Experimental conditions and measurements

The calciner was continuously fed with limestone material for around four days to demonstrate its technical feasibility. During this period, the system logged the power and inner thermocouple temperatures. The steady-state operating conditions of the calciner are summarized in Table 3. It was not practically possible to obtain completely stable conditions, so fluctuations are also included. The operating conditions were chosen based on practical challenges not related to the novel design concept. Increasing the mass flow rate increased the accumulated particles inside the calciner, and the kiln drive motor was not strong enough to rotate the calciner drum. The rotational speed was increased to the maximum level to reduce meal accumulation, and the feeding rate was fixed at a value at which the kiln drive could rotate the rotary drum. The outer shell temperature was measured with an infrared thermometer (BOSCH GIS 1000 C with an accuracy of ±1 °C), and the calcination degree was calculated by measuring the weight loss of the fed limestone and the calcined material (the "loss on ignition" method). The steady-steady condition was verified by continuously measuring the outer shell temperature and calcination degree for 8 h on the last day.

3. Model development

A model of the internally heated calciner was developed and implemented in OpenModelica version 1.19.2. This section covers the mathematical relationships in the model. The mathematical formulation covers notation which is not explained in detail in the text, and the reader is referred to the nomenclature section for explanations. The simulations are performed by dividing the flow direction of the calciner into 500 points.

Table 3
Operating conditions.

Operating parameter	Unit	Value
Limestone feeding rate	kg/h	88 ± 10
Calciner inclination	°	1
Calciner rotational speed	RPM	4
Electrical power input	kW	85.2 ± 0.2
Ambient temperature	°C	30 ± 5
Limestone inlet temperature	°C	30 ± 5
Limestone size	mm	2–8

3.1. Particle characteristics

An XRF analysis of the limestone, in LoI-free oxide form, is shown in the second column in Table 4. For modelling purposes, the composition is back-calculated to a raw composition. It is assumed that all sulfur exists either as potassium sulfate (K_2SO_4) or calcium sulfate ($CaSO_4$). The remaining lime (CaO) after formation of calcium sulfate ($CaSO_4$) is assumed to exist as calcium carbonate ($CaCO_3$). The resulting composition, after normalization to 100%, is shown in the second column in Table 4. Further, other limestone characteristics used for modelling purposes are summarized in Table 5.

3.2. Molar balance

The molar flow rate of component i ($\dot{n}_i$) [mol/s] in the particle flow direction (x-direction) is given by equation (1), assuming steady-state and perfect mixing in the other directions (y and z directions).

$$\frac{d\dot{n}_i}{dx} = \frac{\dot{n}_{i,g}}{l_d} \tag{1}$$

The main chemical reaction in the system is calcite decomposition, as shown in equation (2). The molar generation ($\dot{n}_{i,g}$) term in equation (1) is then given by equation (3).

$$CaCO_3 \rightarrow CaO + CO_2 \tag{2}$$

$$\dot{n}_{i,g} = \gamma_i r_c \tag{3}$$

3.3. Reaction kinetics

The overall reaction rate of calcite decomposition (r_c) depends on three rate-controlling steps, which include 1) heat transfer to the calcite core (including heat transfer through the product CaO layer), 2) calcite decomposition, and 3) mass diffusion of CO_2 through the porous product (CaO) layer [18]. For a particle size in the range of micro-meters, the mass diffusion may be negligible [19], however, since this study deals with bigger particles, the mass diffusion of CO_2 through the product layer may also be important [20].

The reaction kinetics are modelled with a shrinking core model, as shown in Fig. 2. The calcium carbonate core ($CaCO_3$) is assumed to be a sphere that shrinks as the reaction proceeds. A layer of porous lime (CaO) is formed as a product outside the core, and the produced CO_2 has to diffuse through this CaO layer.

The overall reaction rate including the effects of calcite decomposition at the core surface and diffusion of CO_2 through the product CaO layer is shown in equation (4). The reaction starts only when the

Table 4
Limestone composition. The LoI calculated from the XRF analysis is 43.1%.

Component	XRF analysis, LoI-free basis (wt%)	Back-calculated raw composition (wt%)
$CaCO_3$	-	96.5
CaO	94	-
SiO_2	2.7	1.5
Al_2O_3	0.7	0.4
Fe_2O_3	0.5	0.3
MgO	1.4	0.8
K_2O	0.3	-
SO_3	0.4	-
K_2SO_4	-	0.3
$CaSO_4$	-	0.2
Sum	100	100

Table 5
Limestone characteristics used in the model.

Parameters	Value	Units	Remark
Effective emissivity of the limestone (ε_l)	0.69	-	Literature [17]
Approximate density of the limestone (ρ_l)	2700	kg/m^3	Approximate value
Bulk density of the limestone bed (ρ_b)	1426	kg/m^3	Measured
Average initial limestone radius ($R_{C,o}$)	2.5	mm	Measured

equilibrium pressure (given by equation (5) [21]) (p_{eq}) [Pa] becomes higher than the partial pressure of CO_2 at the calcite core surface ($p_{CO2,c}$). Before the reaction starts, the CO_2 partial pressure at the spherical surface ($p_{CO2,c}$) is equal to the partial pressure of CO_2 (p_{CO2}) in the calciner as there is no product layer to create a pressure gradient. The total number of reacting particles (N_{rc}) in equation (4) is derived in Appendix A.

$$r_c = N_{rc} A_C \frac{p_{eq} - p_{CO2}}{\frac{1}{k_{c,r}} + \frac{1}{k_{c,D}}} \tag{4}$$

$$p_{eq} = 4.192 \times 10^{12}\ exp\left(\frac{-20474}{T_C}\right) \tag{5}$$

The rate constant for the calcite decomposition ($k_{c,r}$) is given by equation (6) [22]. In reality, the exposed surface area is higher than the surface area of the (spherical) core (A_C) due to the pores at the calcite surface [18]. The excess area is modelled with an area factor (A_{fac}) which will always be equal to or greater than 1 depending on the porosity of the calcite. The factor is unknown and is used as a fitting parameter in the model.

$$k_{c,r} = 1.22 \times 10^{-5}\ exp\left(\frac{-4026}{T_C}\right) \times A_{fac} \tag{6}$$

The rate constant for the CO_2 diffusion through the lime (CaO) layer ($k_{c,D}$) is found by assuming a steady-state diffusion and solving Fick's diffusion law for a sphere [16] and is given by equation (7).

$$k_{c,D} = \frac{D_{CO2}}{R\,T_C} \times \frac{R_{C,o}}{R_C\left(R_C - R_{C,o}\right)} \tag{7}$$

The overall diffusivity of CO_2 through porous lime (D_{CO2}) depends on the molecular diffusivity (D_M) and the Knudsen diffusivity (D_K) and is given by equation (8) [20]. Here, τ_p is the tortuosity factor (found to be 1.5 in previous work [23]) and ε_{CaO} is the porosity of the particle (assuming that lime is produced from non-porous carbonate with negligible particle shrinkage; the theoretical value is 0.55 [24]).

$$\frac{1}{D_{CO2}} = \frac{{\tau_p}^2}{\varepsilon_{CaO}} \left(\frac{1}{D_M} + \frac{1}{D_K}\right) \tag{8}$$

The molecular diffusivity (D_M) is further given by equation (9) [25] and the Knudsen diffusivity (D_K) is given by equation (10) [26]. In the equations, σ_{CO2} is the effective collision diameter of CO_2 [Å] and is equal to 3.941 [25]. The collision integral (ω_D) is available in tabular form in the literature [25] and is fitted into equation (11) with the fitting results shown in Fig. 3. The pore radius in the product layer, r_{pore}, depends on the degree of sintering and the initial limestone porosity. Stanmore and Gilot [24] commented in their review on calcination that the pore radius should be around 50 nm, so this value is used in this study.

$$D_M = 1883 \times 10^{-5} \frac{T_C^{1.5} (2/M_{CO2})^{0.5}}{p_{avg} \sigma_{CO2}^2 \omega_D} \tag{9}$$

$$D_K = 9.7 r_{pore} \sqrt{\frac{T_C}{M_{CO2}}} \tag{10}$$

$$\omega_D = 0.67 + \frac{164}{T_C} - \frac{2778}{{T_C}^2} \tag{11}$$

3.4. Energy balance

Assuming steady-state conditions inside the calciner, the change in total enthalpy ($\dot{H}$) in the flow direction (x-direction) is shown in equation (12), in which $\dot{q}_b$ is the total energy transferred to the particle bed from all sources, and this energy is responsible for the enthalpy (and thereby temperature) rise of the flowing particles.

$$\frac{d\dot{H}}{dx} = \frac{\dot{q}_b}{l_d} \tag{12}$$

The total enthalpy is further given by equation (13), where H_i is the specific enthalpy of each component [J/mol] and is a function of particle core temperature (T_C) (detailed equations are given in Appendix B).

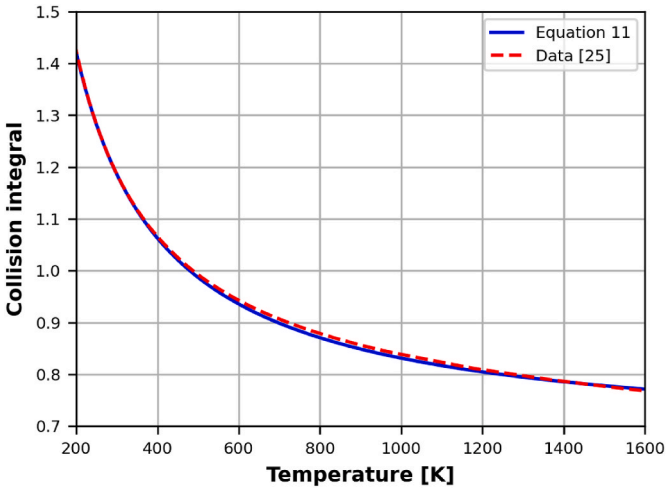

Fig. 3. Fitting collision integral for CO_2 gas into equation (11) based on published data [25].

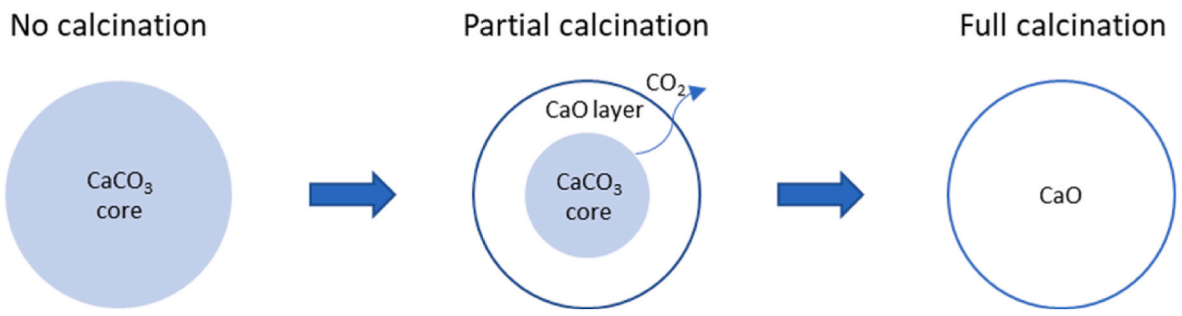

Fig. 2. Schematic of a shrinking core model.

$$\dot{H} = \sum \dot{n}_i H_i \tag{13}$$

3.5. Heat transfer

At steady-state conditions, the total heat generated in the elements ($\dot{q}_e$) [W] is either transferred to the particle bed ($\dot{q}_b$) or lost to the environment ($\dot{q}_L$) as per equation (14). Each of the aspects of heat transfer is covered in the sub-sections.

$$\dot{q}_e = \dot{q}_b + \dot{q}_L \tag{14}$$

3.5.1. Heat generated in heating elements

The heat is generated by ohmic heating, and the conversion of electricity to heat is not 100% efficient due to heat generated during power control and at the terminals. The efficiency (η_e) is assumed to be 95% [27], and heat generated in the elements ($\dot{q}_e$) is given by equation (15).

$$\dot{q}_e = P_e \eta_e \tag{15}$$

3.5.2. Heat transfer to the particle bed

The heat transferred to the bed ($\dot{q}_b$) comes either via the covered bed ($\dot{q}_{cb}$) or via the exposed bed ($\dot{q}_{eb}$) as shown in equation (16) and Fig. 4. The exposed bed is heated up with a combination of net radiation heat transfer from heating elements and convective heat transfer from the gas. The covered bed is heated by convection and radiation from the covered inner drum.

$$\dot{q}_b = \dot{q}_{eb} + \dot{q}_{cb} \tag{16}$$

The convective heat transfer from the gas to the exposed bed is assumed to be negligible compared to radiation heat transfer as the gas flow rate is relatively low and the temperature is high. Radiation heat transfer to the exposed bed is a complex process with interactions between the element, bed, inner drum, and gas. The problem is solved with a network approach, as shown in Fig. 5.

Fig. 5 shows the transfer of heat from the heating element ($\dot{q}_e$) to the exposed bed ($\dot{q}_{eb}$) and to the inner drum ($\dot{q}_d$). The gas is assumed to be re-radiating as most of the radiating part of the gas is enclosed between the element, the inner drum, and the bed. The heat transferred to the drum is either transferred to the covered bed ($\dot{q}_{cb}$) or lost to the environment ($\dot{q}_L$). The radiation network can then be solved by simultaneously solving equations (17)–(20).

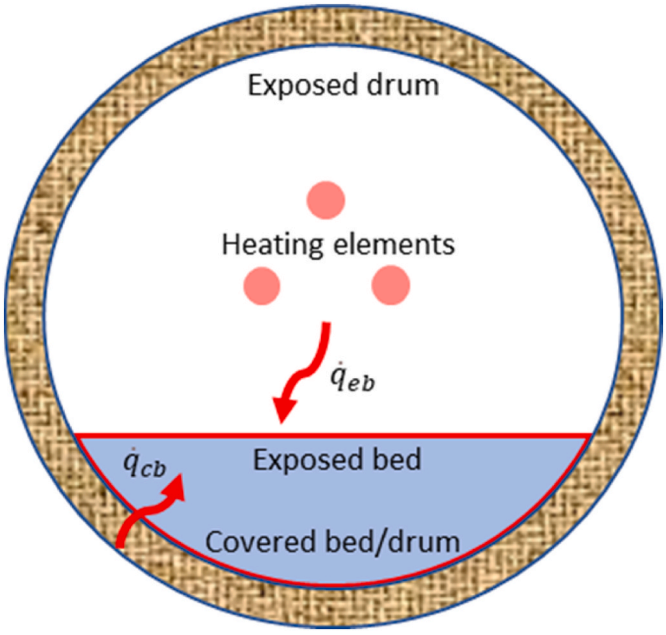

Fig. 4. Pathways for heat transfer to the bed.

$$\frac{J_g - J_e}{R_3} + \frac{J_g - J_d}{R_6} + \frac{J_g - J_b}{R_9} = 0 \tag{17}$$

$$\frac{J_e - J_d}{R_2} + \frac{J_e - J_g}{R_3} + \frac{J_e - J_b}{R_4} = \frac{\sigma T_e^4 - J_e}{R_1} = \dot{q}_e \tag{18}$$

$$\frac{J_b - J_e}{R_4} + \frac{J_b - J_d}{R_7} + \frac{J_b - J_g}{R_9} = \frac{\sigma T_b^4 - J_b}{R_8} = \dot{q}_{eb} \tag{19}$$

$$\frac{J_d - J_e}{R_2} + \frac{J_d - J_g}{R_6} + \frac{J_d - J_b}{R_7} = \frac{\sigma T_{d,i}^4 - J_d}{R_5} = \dot{q}_d = \dot{q}_{cb} + \dot{q}_L \tag{20}$$

The parameters required to solve the network resistance (R_1 to R_9) are derived in Appendix C. Since the gas is assumed to be re-radiating, the gas radiosity is equal to black-body radiation and the gas temperature (T_g) is given by equation (21).

$$T_g = \left(\frac{J_g}{\sigma}\right)^{0.25} \tag{21}$$

The heat transferred to the covered bed ($\dot{q}_{cb}$) is given by equation (22). The heat transfer coefficient in the covered bed (h_{cb}) is given by equation (23) [28]. The effective bed conductivity (k_b) is 0.14 W/(m^{2}K) for calcite [29].

$$\dot{q}_{cb} = h_{cb} A_{cd} \left(T_{d,i} - T_b\right) \tag{22}$$

$$h_{cb} = \frac{11.6\, k_b}{R_{d,i}\Gamma} \left(\frac{\Gamma N {R_{d,i}}^2}{\alpha_b}\right)^{0.3} \tag{23}$$

The heat transferred to the bed must flow through the lime (CaO) layer to reach the calcite core, and this is given by equation (24) by assuming conduction heat transfer through a sphere [16]. The thermal conductivity of the produced lime (k_C) is found to be 0.6 W/(m·K) in the literature [23].

$$\dot{q}_b = \dot{q}_{eb} + \dot{q}_{cb} = \frac{4\pi k_C N_{rc} (T_b - T_C)}{(1/R_C) - \left(1/R_{C,o}\right)} \tag{24}$$

3.5.3. Heat loss to the environment

The heat lost to the environment ($\dot{q}_L$) is due to conduction via the calciner drum and then free convection and radiation from the outer drum surface. The overall effect is given by equation (25).

$$\dot{q}_L = \frac{T_{d,i} - T_a}{\frac{\ln\left(d_{d,o}/d_{d,i}\right)}{2\pi k_d . l_d} + \frac{1}{A_{d,o} h_L}} \tag{25}$$

The overall heat loss coefficient (h_L) is the sum of the radiation coefficient ($h_{L,R}$) and the convection coefficient ($h_{L,C}$) for the outer surface, as shown in equations (26)–(28). The view factor from the external surface of the calciner to the environment is 1 as it is fully visible to the isothermal environment. So, this parameter is not included in equation (27). The estimation of parameters such as Nusselt number (Nu_D) and thermal conductivity of air (k_a) in equation (28) is described in detail in Appendix D.

$$h_L = h_{L,R} + h_{L,C} \tag{26}$$

$$h_{L,R} = \sigma \times \varepsilon_{d,o} \times \left({T_{w,out}}^2 + {T_{amb}}^2\right)\left(T_{w,out} + T_{amb}\right) \tag{27}$$

$$h_{L,C} = \frac{Nu_D k_a}{d_{d,o}} \tag{28}$$

3.5.4. Overall heat transfer coefficient

The overall heat transfer coefficient (U) based on the heating element area is calculated for the heat transfer from the heating elements to the

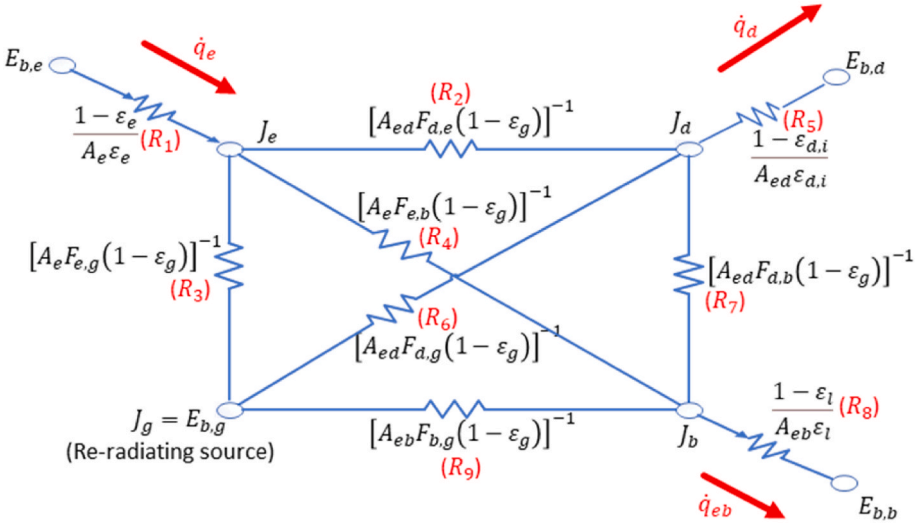

Fig. 5. Radiation heat transfer network to find heat transferred to the exposed bed.

calcite core, and it is calculated from equation (29).

$$U = \frac{\dot{q}_b}{A_e(T_e - T_C)} \tag{29}$$

4. Results and discussions

4.1. Concept demonstration

The novel calciner design was successfully demonstrated at a feeding rate of around 88 kg/h. The test campaign lasted approximately four days, and the measured parameters are shown in Fig. 6. The operation conditions were relatively stable after the start-up phase. So, the concept is technically feasible for calcining coarse limestone particles.

4.2. Comparison of modelling and experimental results

The outer drum temperature was measured every 30 min for 8 h on the last day of the test campaign. The measured outer drum temperature and the model predictions of the temperature profile are shown in Fig. 7. A comparison of calcination degree from the experiments and from the model is shown in Fig. 8. Due to the process fluctuations shown in Table 3, the experimental results on outer wall temperature and calcination degree also fluctuated for each measurement, and these fluctuations are included in Figs. 7 and 8, respectively. The modelled results match quite well and are within the uncertainty range of experimental results. The bed temperature increases until the calcination temperature is reached. Once the calcite in the bed starts to calcine, the bed temperature becomes almost constant as the heat of reaction is counterbalanced by heat transferred to the bed. The other temperature profiles can be explained with the help of heat flow results, which are discussed in the next section.

4.3. Heat transfer inside the calciner

The heat transfer per length of the calciner is shown in Fig. 9.

Via the electricity-to-heat conversion around 5% of the input power is lost (see section 3.5.1). Out of the remaining 95% of the power input, around 40% is transferred to the meal and 55% is lost to the environment. The heat transfer to the bed is highest at the inlet region, as in this region the bed temperature is lowest; the higher temperature gradient gives a higher heat transfer rate. A consequence of the high heat transfer rate in the inlet region is a lower temperature of the heating element and the drum (see Fig. 7). Low temperatures at the inlet also reduce the heat losses (convection and radiation from the outer drum) in this region. In contrast to the inlet region, the outlet region shows the opposite effect. The heat transfer to the bed at the outlet region becomes lower due to a higher bed temperature (and lower temperature gradient). Further, heat losses dominate in the exit region due to higher outer drum temperatures. Even though the heat loss is high for the experimental calciner, a better choice of refractory materials (with lower thermal conductivity) and steel shell (with lower emissivity) could reduce the heat loss significantly. This aspect is studied in the next section.

The heat transfer contribution from the exposed and covered bed is

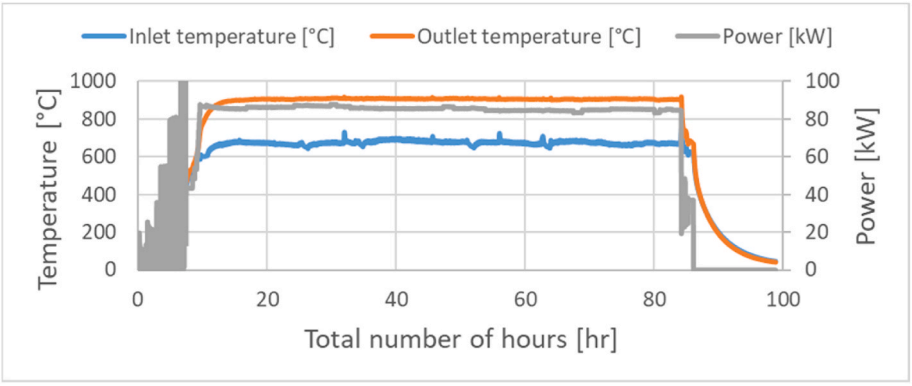

Fig. 6. Measured parameters during the operating period of the calciner.

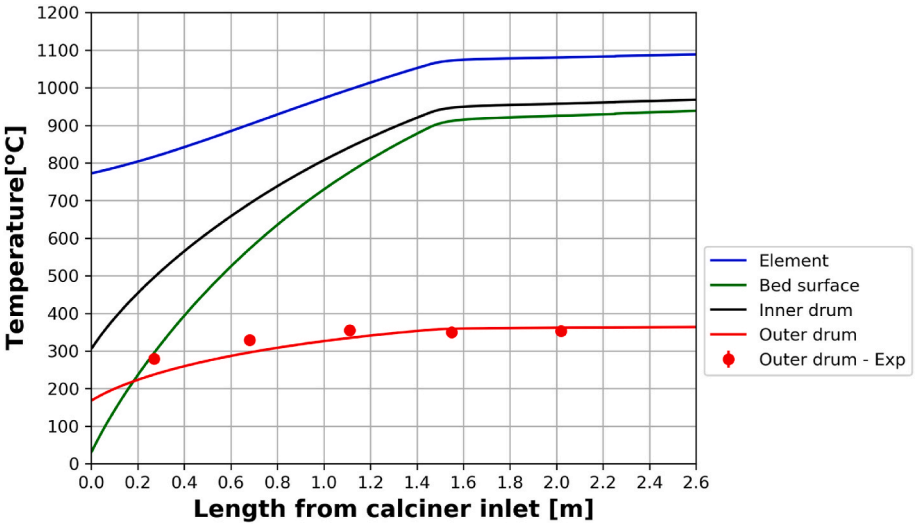

Fig. 7. Temperature profile inside the internally heated rotary calciner.

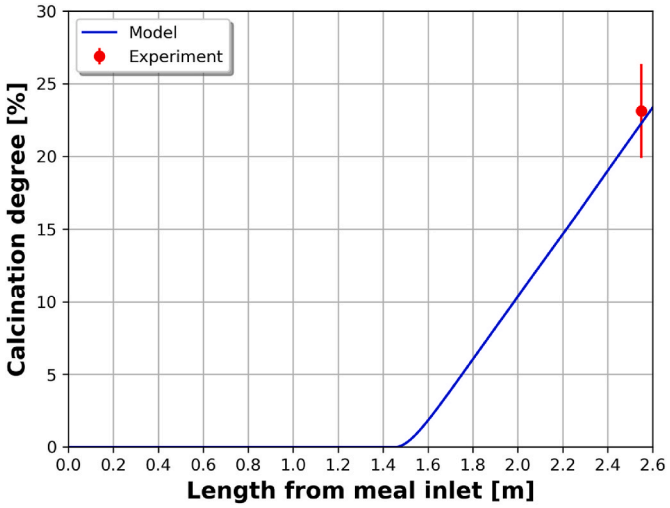

Fig. 8. Calcination degree profile inside the internally heated rotary calciner.

shown in Fig. 10. Close to the calciner inlet, the heat transfer contribution from the covered bed is much higher than from the exposed bed. The heat loss is much lower in the inlet region due to low temperatures, so most heat transferred to the inner drum goes to bed. However, this changes in the outlet region as the bed temperature increases and the heat loss increases. Due to the high heat loss, a lower fraction of heat is transferred to the covered bed. So, the heat transferred from the exposed bed becomes a much more significant contributor to the heat transfer process.

The overall heat transfer coefficient to the calcite core is further shown in Fig. 11. The heat transfer coefficient lies between 69 and 110 W/(m^{2}K), with an average value of 101 W/(m^{2}K). The overall heat transfer coefficient initially increases due to an increased effect of radiation from higher bed temperatures. However, the onset of calcination produces an additional heat transfer resistance due to the porous product layer formed outside the calcite shell. So, the heat transfer coefficient also decreases accordingly.

4.4. *Potential for process improvement*

A step-by-step procedure to improve energy efficiency is shown in Table 6.

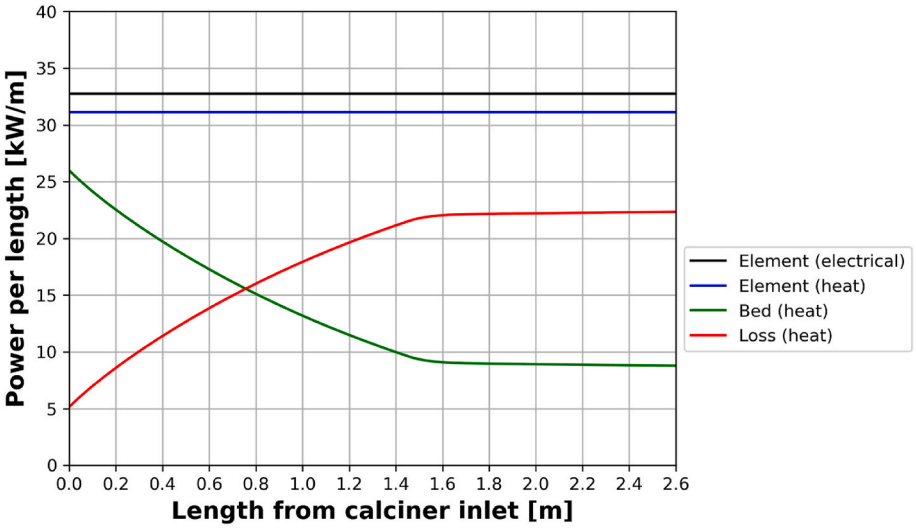

Fig. 9. Power profile inside the internally heated rotary calciner.

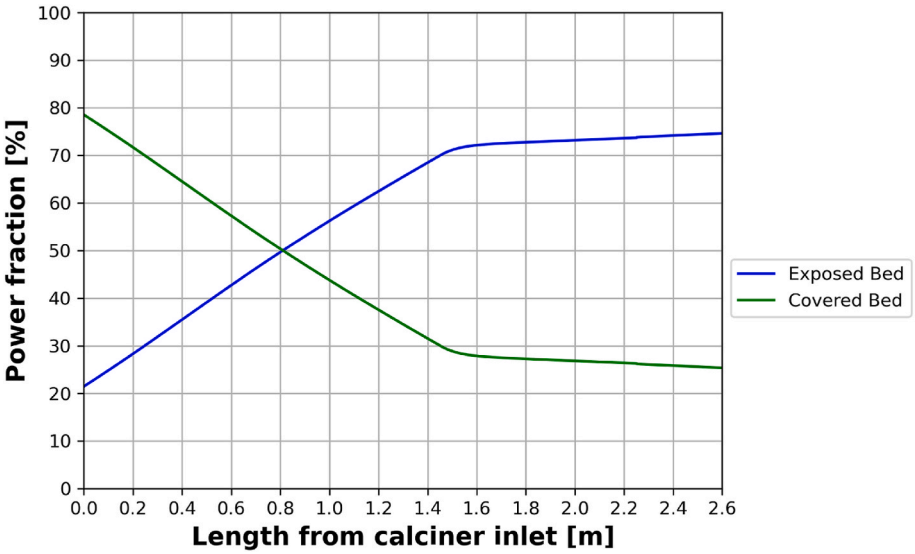

Fig. 10. Fraction of power transferred to the exposed and the covered bed.

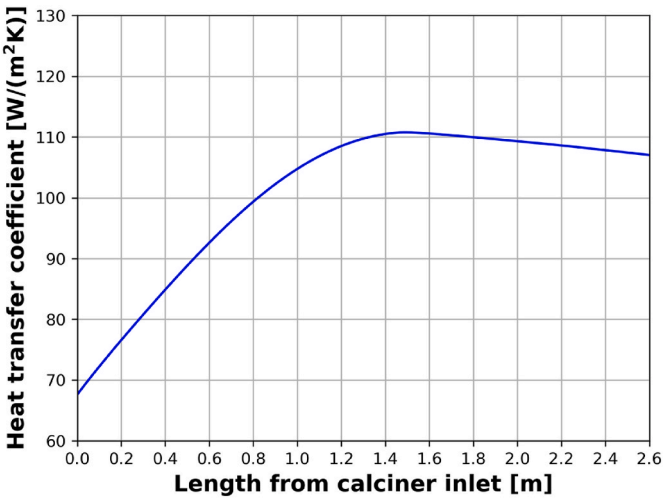

Fig. 11. Overall heat transfer coefficient for heat transfer to the calcite core.

Table 6
Step-by-step procedure to improve energy efficiency.

Step No.	Design/Operation change	Calcination degree [%]	Total loss [%]	Maximum element temperature [°C]
0	Base case (studied experimentally)	23	60	1089
1	Reduced emissivity of outer shell to 0.19 from 0.88.	44	50	1142
2	Reduced thermal conductivity of drum to 0.21 from 1.2 W/(m.K).	93	21	1504
3	Reduced inclination and rotational speed to 0.5° and 1 RPM from 1° to 4 RPM.	100	20	1362
4	Increasing feeding rate and input power to 120 kg/h and 102 kW from 88 kg/h and 85.2 kW	90	17	1235
5	Increasing wall thickness to 0.18 m from 0.065 m.	98	11	1320

The first objective is to reduce energy loss, as 60% of the energy is lost in the current setup. In the first step, radiation heat loss is reduced by reducing the emissivity of the outer shell. Changing the outer shell material to polished stainless steel can reduce the emissivity to 0.19 (emissivity at 327 °C [16]). With this step, the calcination degree increases to 44%, and the heat loss drops to 50%. In the second step, the heat loss through the wall is reduced by reducing the thermal conductivity of the shell material. Heat loss can also be reduced by implementing composite walls. However, to keep things simple, only the thermal conductivity of the shell material is changed here. Material such as "Keiselguhr" can tolerate up to 1000 °C and has a thermal conductivity of 0.21 W/(m·K) at 800 °C [30]. Reducing the thermal conductivity to 0.21 W/(m·K) further reduces the heat loss to 21% and increases the calcination degree to 93%. However, the maximum element temperature increases to 1504 °C, which is above the maximum recommended operating temperature of silicon carbide (around 1400 °C [31]). The heat efficiency can be improved further by increasing the residence time of particles, as done in the third step. Increasing the residence time reduces the diffusion/thermal resistance effect by the product lime layer. The calcination inclination and rotational speed are reduced to 0.5° and 1 RPM, respectively, to reduce the residence time. With these settings, the calcination degree increases to 100%, and the heat loss is reduced to 20%. The maximum element temperature in the final step is also below 1400 °C, which is the maximum recommended operating temperature of silicon carbide [31]. To further improve the efficiency, the feeding rate can be increased to 120 kg/h, and the power can be increased to 102 kW (i.e. full power) in the fourth step, as the limestone feed in the third step was fully calcined. With the increased power and feeding rate, the loss is reduced to 17%, and the calcination degree becomes 90%. In the final step, the heat loss is further reduced by increasing the shell thickness to 0.18 m. At this step, the calcination degree increases to 98%, and the heat loss is reduced to 11%.

The environmental and economic impact of increasing heat efficiency by the procedure described in Table 6 is shown in Fig. 12. The electricity cost was calculated by assuming an electricity cost of 0.5 NOK/kWh, which was the electricity cost in Norway in fourth quarter of 2022 for energy-intensive manufacturing units [32]. The electrified calciner produces relatively pure CO_2, so there is no need for CO_2 capture (e.g. by amine absorption). So, the results are shown in terms of CO_2 units. The energy intensity on produced CO_2 is reduced from 35 MJ/kg-CO_2 to 7 MJ/kg-CO_2 (i.e., a reduction of 79%) by reducing the heat loss from 60% to 11%. The corresponding electricity cost per kg CO_2 is also reduced from 4.9 to 1 NOK/kg-CO_2. The results show an

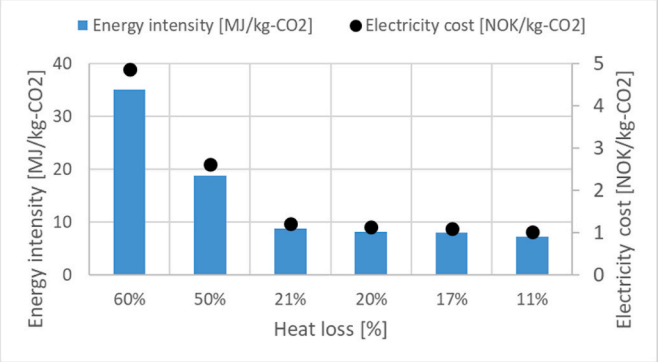

Fig. 12. Comparison of energy intensity and electricity cost per kg CO_2 produced for different heat loss at each step shown in Table 6.

improved environmental impact as a larger amount of pure CO_2 can be sent for storage with the same energy and the economic impact as the cost per unit of CO_2 reduces.

4.5. Advantages and disadvantages of the concept

The advantages and disadvantages of an axially heated rotary calciner are discussed based on the operational experience. The advantages of the concept include:

1. The operation of the calciner is very smooth, and the temperatures and calcination degree can be controlled very accurately.
2. It should be easy to retrofit an existing rotary kiln as the heating elements could replace the fuel firing system (see Fig. 13).
3. The wall drum can be made from inexpensive steel and refractory materials, avoiding high costs and heat losses.
4. The heating elements can be operated at very high temperatures, thereby achieving a high radiation heat transfer.

The disadvantages and uncertainties of the concept include:

1. The concept is new, and the choice of the internal heating element material is not extensively studied. This study uses silicon carbide as this material is rigid at high temperature. However, silicon carbide has an aging problem, wherein the resistivity of the heating elements increases over time [30,31]. The voltage across the heating elements could be increased with a transformer to compensate for the increased resistance. However, the extent of voltage increase is limited, possibly reducing the lifetime of the elements. So, the maintenance cost could be high.
2. Dust particles can accumulate on top of the heating elements, thereby reducing the local heat transfer from the elements. This effect may cause the dust-insulated area to reach a higher temperature than the non-insulated area of the heating elements. If the temperature difference becomes significant, the thermal expansion in the local region may differ too much and cause the element to break. This effect was partly observed during the experiments. Due to the dust accumulation causing the higher temperature on the upper part, the upper part expanded more than the lower part. This caused the element to bend slightly upwards (see the shape of the heating elements inside the calciner in Fig. 13).

5. Conclusions

This study covers the design of an electrically heated rotary calciner with internal heating. All the previous studies employed external heating on the electrically heated rotary calciner. So, internal heating is the new concept studied in this work. The internally heated system can utilize the rotary drum material from a regular fuel-fired rotary calciner. So, unlike an externally heated system, special materials with high thermal conductivity on the drum material are not needed.

The novel design was first operated continuously for four days, and the concept was found to be technically feasible. The outer shell temperature and calcination degree were continuously measured during the last 8 h of operation, and the results showed that the system was close to a pseudo-steady state.

A 1-D steady-state model of the calciner was developed and implemented in OpenModelica version 1.19.2. The simulation results were compared against the measured outer shell temperature and calcination degree during the last 8 h of operation. The simulation results matched well within the uncertainty range of the measured outer shell temperature and calcination degree. Hence, the model was found to be suitable for analyzing the heat transfer process and recommending pathways for process improvements. The modelling results of the current setup showed that:

1. Around 60% of the total input electrical energy is lost in the current setup.

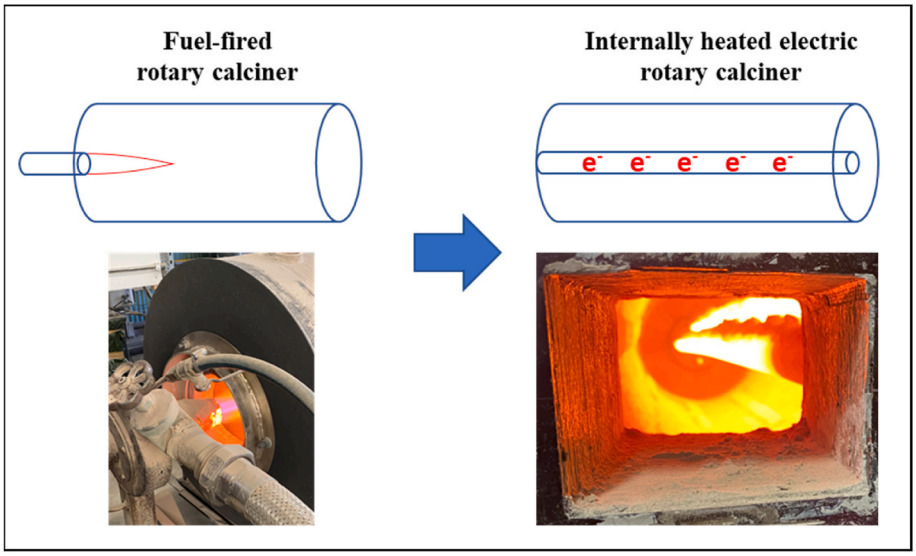

Fig. 13. Transformation of fuel-fired rotary calciner to an internally heated electric rotary calciner.

2. The heat transferred to the bed was higher than the heat loss at the inlet region, while heat loss dominated the exit region.
3. The heat transfer from the covered bed accounted for around 80% of the total heat transfer at the inlet region. In contrast, at the exit region, the exposed bed dominated and contributed to around 80% of the heat transfer.
4. The average heat transfer coefficient was calculated to be 101 W/(m^2K). Due to increased radiation, the heat transfer coefficient increased until the calcination started. In the calcination region, however, the heat transfer coefficient was slightly reduced due to the presence of the product layer.

The main problem with the current setup is a very low thermal efficiency, as the total loss from the system amounted to around 60%. A step-by-step procedure was therefore developed to reduce the heat loss from 60% to around 11%. The improved heat efficiency was achieved with a combination of improved insulation of the drum wall, reduced radiative emission from the outer shell, and increased residence time of the particles. The energy intensity of the produced CO_2 (which can be directly captured as it is relatively pure) was thereby reduced from 35 to 7 MJ/kg-CO_2. The cost per unit of CO_2 was also reduced from 4.9 to 1 NOK/kg-CO_2. So, an improved efficiency also improves the economy of the process.

The advantages and disadvantages of the concept are discussed based on operational experience. The concept has several advantages, such as smooth operation, easy retrofitting, and a quite high radiation heat transfer. However, it also has some challenges, such as the choice of heating element. The silicon carbide material used in this study has a limited lifetime, which can significantly increase the operating cost. Further, dust accumulation on the heating elements can cause a local temperature rise which may cause an uneven thermal expansion over the heating tube cross-section, and this may lead to heating element failure in the worst-case scenario.

Credit author statement

Ron M Jacob: Conceptualization, Methodology, Software, Validation, Investigation, Writing – original draft, Visualization. Lars-André Tokheim: Conceptualization, Methodology, Validation, Investigation, Writing – review & editing, Visualization, Supervision, Project administration, Funding acquisition.

Declaration of competing interest

The authors declare that they have no known competing financial interests or personal relationships that could have appeared to influence the work reported in this paper.

Data availability

Data will be made available on request.

Acknowledgment

This study was supported by the “ELSE 2” project, a Norwegian research project on electrified cement production. The project is funded partly by Norcem AS and CLIMIT (a Norwegian CCS Research Program, Project number: 620035), and they are greatly acknowledged. The calciner was constructed at Cementa’s plant in Slite, Sweden, with help from AFRY and Kanthal. They are also acknowledged for their support. Further, we are thankful to the staff at Cementa and Kanthal for their constant support in conducting the experiments in a reliable way. This work was conducted in parallel with a project at Stockholm University, where the produced lime is used in the project Levende Hav AB. So, they are also acknowledged for their support.

Appendix A. Mass accumulation inside the calciner

The cross-sectional view of the calciner without heating elements is shown in Fig. A-1.

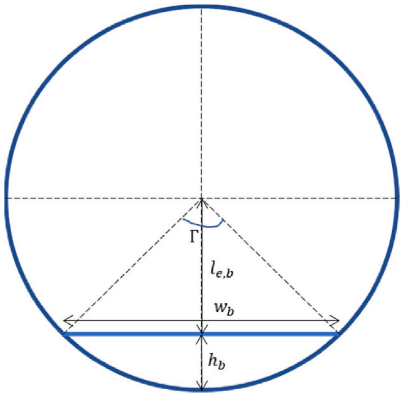

Fig. A-1. Cross-sectional view of the calciner without heating elements.

The angle subtended by the particle flow (Γ) [radian] is dependent on the operating condition and can be given by equation A-1 [33].

$$\Gamma = 2\,sin^{-1}\left(\frac{4\dot{m}/\rho_b}{\pi {d_{d,i}}^3 N\,sin(\gamma)sin(\omega+\omega_o)}\right)^{1/3} \quad \text{(A-1)}$$

In equation A-1, the angle of repose (γ) is assumed to be 35° for limestone [33], and the extra angle (ω_o) formed by the particle bed is a fitting parameter based on experimental results. The average bed height (h_b), perpendicular length of element to bed ($l_{e,b}$), bed width (w_b), particle flow area (A_{pf}), mass of the accumulated bed (m_b), and number of reacting particles (N_{rc}) are given in equation A-2 to A-7.

$$h_b = \frac{d_{d,i}}{2} - \frac{d_{d,i}}{2} cos\left(\frac{\Gamma}{2}\right) \tag{A-2}$$

$$l_{e,b} = \frac{d_{d,i}}{2} cos\left(\frac{\Gamma}{2}\right) \tag{A-3}$$

$$w_b = 2\sqrt{\left(\frac{d_{d,i}}{2}\right)^2 - \left(\frac{d_{d,i}}{2} cos\left(\frac{\Gamma}{2}\right)\right)^2} \tag{A-4}$$

$$A_{pf} = \frac{\Gamma}{2}\left(\frac{d_{d,i}}{2}\right)^2 - w_b \frac{d_{d,i}}{4} cos\left(\frac{\Gamma}{2}\right) \tag{A-5}$$

$$m_b = \rho_b A_{pf} l_d \tag{A-6}$$

$$N_{rc} = \frac{m_b x_c}{(4/3)\,\pi\, R_{C,o}^3\, \rho_l} \tag{A-7}$$

Appendix B. Thermodynamic properties used in the model

The components included in the model are summarized in Table B-1. Different model types in Table B-1 use different models to predict the specific heat capacity and these models are summarized in Table B-2. The polynomial coefficients of the specific heat coefficient are estimated by fitting specific heat data available in Barin's handbook [34]. The enthalpy equation is derived by integrating equation B-1, and the derived polynomial equation is shown in Table B-3. Finally the fitted polynomial coefficients are shown in Table B-4.

$$H - H_{ref} = \int_{T_{ref}}^{T} C_P(T_C) dT_C \tag{B-1}$$

In equation B-1, H is the enthalpy at a given temperature [J/mol], H_{ref} is the standard enthalpy (values are shown in Table B-5) [J/mol], and $C_P(T_C)$ is the polynomial equation for specific heat [J/mol-K].

Table B-1
Components and model types.

Model type	Components
Solid model 1	$CaCO_3$, CaO, SiO_2, Al_2O_3, Fe_2O_3, MgO, $CaSO_4$
Solid model 2	K_2SO_4
Gas model 1	CO_2

Table B-2
The specific heat equation for each model type.

Model type	Specific heat equation [J/mol-K]
Solid model 1	$C_p = C_1 + C_2 T_C + C_3 T_C^2 + C_4 T_C^3 + C_5 T_C^4$ $C_6 \le T_C \le C_7$
Solid model 2	$C_p = C_1 + C_2 T_C + C_3 T_C^2 + \frac{C_4}{T_C} + \frac{C_5}{T_C^2} + \frac{C_6}{T_C^{0.5}}$ $C_7 \le T_C \le C_8$
Gas model 1	$C_p = C_1 + C_2\left(\frac{C_3/T_C}{\sinh(C_3/T_C)}\right)^2 + C_4\left(\frac{C_5/T_C}{\cosh(C_5/T_C)}\right)^2$ $C_6 \le T_C \le C_7$

Table B-3
The enthalpy equation for each model type.

Model type	Specific heat equation [kJ/mol]
Solid model 1	$H - H_{ref} = C_1(T_C - T_{ref}) + \frac{C_2(T_C^2 - T_{ref}^2)}{2} + \frac{C_3(T_C^3 - T_{ref}^3)}{3} + \frac{C_4(T_C^4 - T_{ref}^4)}{4} + \frac{C_5(T_C^5 - T_{ref}^5)}{5}$ $C_6 \le T_C \le C_7$
Solid model 2	$H - H_{ref} = C_1(T_C - T_{ref}) + \frac{C_2(T_C^2 - T_{ref}^2)}{2} + \frac{C_3(T_C^3 - T_{ref}^3)}{3} + C_4 \ln\left(\frac{T_C}{T_{ref}}\right) - C_5\left(\frac{1}{T_C} - \frac{1}{T_{ref}}\right) + \frac{C_6(T_C^{0.5} - T_{ref}^{0.5})}{0.5}$ $C_7 \le T_C \le C_8$
Gas model 1	$H - H_{ref} = C_1(T_C - T_{ref}) + C_2 C_3\left[\coth\left(\frac{C_3}{T_C}\right) - \coth\left(\frac{C_3}{T_{ref}}\right)\right] - C_4 C_5\left[\tanh\left(\frac{C_5}{T_C}\right) - \tanh\left(\frac{C_5}{T_{ref}}\right)\right]$ $C_6 \le T_C \le C_7$

Table B-4
Coefficients in the equations for specific heat/enthalpy (the temperature unit is in K).

Comp	C_1	C_2	C_3	C_4	C_5	C_6	C_7	C_8
$CaCO_3$	-2.3728	0.4622	-0.000735	5.57E-07	-1.57E-10	298	1200	-
CaO	23.0403	0.09213	-0.00010746	5.716E-08	-1.11E-11	298	1900	-
SiO_2	-8.469	0.252	-0.000296	1.518E-07	-2.84E-11	298	1900	-
Al_2O_3	2.495	0.3665	-0.000422	2.208E-07	-4.25E-11	298	1900	-
Fe_2O_3	51.836	0.153	0.00014	-2.910E-07	1.03E-10	298	1700	-
MgO	13.42	0.114	-0.00013	6.94E-08	-1.33E-11	298	1900	-
K_2SO_4	3782.9	-1.0257	0.000166	1.47E+06	-6.66E+07	-130,297	298	1900
$CaSO_4$	96.2	-0.066	0.000336	-2.55E-07	5.75E-11	298	3000	-
CO_2	53.7	9.95	1887.73	-41.5	-273.6	298	3000	-

Table B-5
Standard enthalpy of the components (at 25 °C and 1 bar).

Component	Standard enthalpy (H_{ref}) [J/mol]	Component	Standard enthalpy (H_{ref}) [J/mol]
$CaCO_3$	-1206,921	**MgO**	-601241
CaO	-635,089	**Fe2O3**	-824,248
CO_2	-393,505	**K2SO4**	-1437,790
SiO_2	-910,857	**CaSO4**	-1434,108
Al_2O_3	-1675,692		

Appendix C. Estimation of parameters to solve the radiation network

The unknown parameters in the radiation network (see Fig. 5) are summarized in Table C-1.

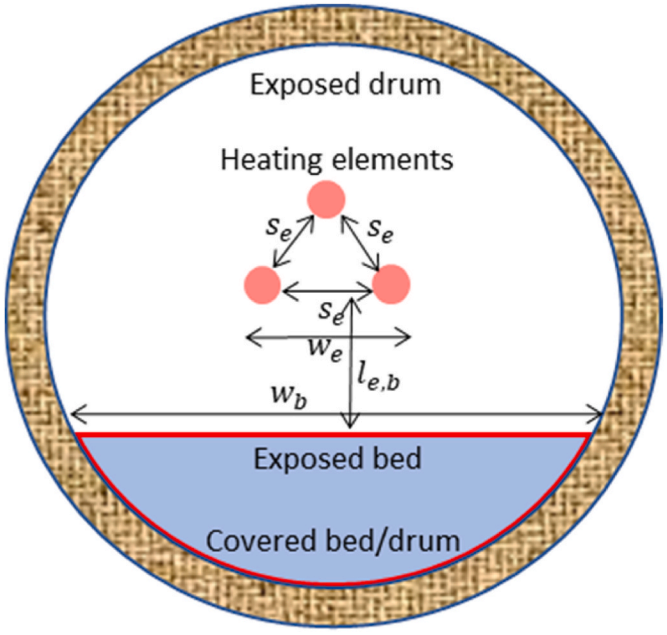

Fig. C-1. Geometrical configuration of the calciner cross-section with heating elements.

Table C-1
Summary of unknown parameters required to solve the radiation network.

Parameters	Symbol	Equation/Value	Remarks
View factor from element to element	$F_{e,e}$	Equation C-1	Infinitely long parallel cylinders [35]
View factor from element to bed	$F_{e,b}$	Equation C-2	Parallel plates with different width [35]
View factor from bed to element	$F_{b,e}$	Equation C-3	Reciprocity rule
View factor from element to drum	$F_{e,d}$	Equation C-4	Summation rule
View factor from drum to element	$F_{d,e}$	Equation C-5	Reciprocity rule

(*continued on next page*)

Table C-1 (*continued*)

Parameters	Symbol	Equation/Value	Remarks
View factor from bed to drum	$F_{b,d}$	Equation C-6	Summation rule
View factor from drum to bed	$F_{d,b}$	Equation C-7	Reciprocity rule
View factor from bed to bed	$F_{b,b}$	0	Bed surface cannot view itself
View factor from element to gas	$F_{e,g}$	1	Fully visible to gas
View factor from drum to gas	$F_{d,g}$	1	Fully visible to gas
View factor from bed to gas	$F_{b,g}$	1	Fully visible to gas
Width of element	w_e	Equation C-8	Derived
Area of exposed drum	A_{ed}	Equation C-9	Derived
Area of exposed bed	A_{eb}	Equation C-10	Derived
Area of covered drum	A_{cd}	Equation C-11	Derived
CO_2 gas emissivity	ε_g	0.15	Approximate value from Figure C-2

$$F_{e,e} = \frac{2}{\pi}\left(\sqrt{\left(\frac{d_e + s_e}{d_e}\right)^2 - 1} + \sin^{-1}\left(\frac{d_e}{d_e + s_e}\right) - \left(\frac{d_e + s_e}{d_e}\right)\right) \tag{C-1}$$

$$F_{e,b} = \frac{\sqrt{\left(\frac{w_e}{l_{e,b}} + \frac{w_b}{l_{e,b}}\right)^2 + 4} - \sqrt{\left(\frac{w_b}{l_{e,b}} - \frac{w_e}{l_{e,b}}\right)^2 + 4}}{2\left(w_e / l_{e,b}\right)} \tag{C-2}$$

$$F_{b,e} = \frac{A_e}{A_{eb}} F_{e,b} \tag{C-3}$$

$$F_{e,d} = 1 - F_{e,e} - F_{e,b} \tag{C-4}$$

$$F_{d,e} = \frac{A_e}{A_{ed}} F_{e,d} \tag{C-5}$$

$$F_{b,d} = 1 - F_{b,b} - F_{b,e} \tag{C-6}$$

$$F_{d,b} = \frac{A_{eb}}{A_{ed}} F_{b,d} \tag{C-7}$$

$$w_e = s_e + (2d_e) \tag{C-8}$$

$$A_{ed} = l_d\ (\pi - \Gamma)\ d_{d,i} \tag{C-9}$$

$$A_{eb} = l_d\ w_p \tag{C-10}$$

$$A_{cd} = \left(\pi\ d_{d,i}\ l_d\right) - A_{ed} \tag{C-11}$$

The emissivity of CO_2 (ε_g) is a function of gas temperature (T_g) [K] and the product of pressure and characteristic length (pL) [m·atm], as shown in equation C-12 [36]. The constants in equation C-12 are shown in Table C-2. Further, the characteristic length for a cylinder is given by $L = 0.95 d_{d,i}$ [16]. At ambient pressure, the product of the characteristic length and the pressure is 0.551 m atm. With this value, the variation of CO_2 emissivity based on equation C-12 is shown in Fig. C-2.

$$\log\left(\overline{\varepsilon_g T_g}\right) = a_0 + a_1 \log(pL) + a_2 \log^2(pL) + a_3 \log^3(pL) \tag{C-12}$$

Table C-2
Constants to predict CO_2 emissivity [36].

Gas temperature [T_g] [K]	a_0	a_1	a_2	a_3
1000	2.2661	0.1742	-0.039	0.004
1500	2.3954	0.2203	-0.0433	0.00562
2000	2.4104	0.2602	-0.0651	-0.00155

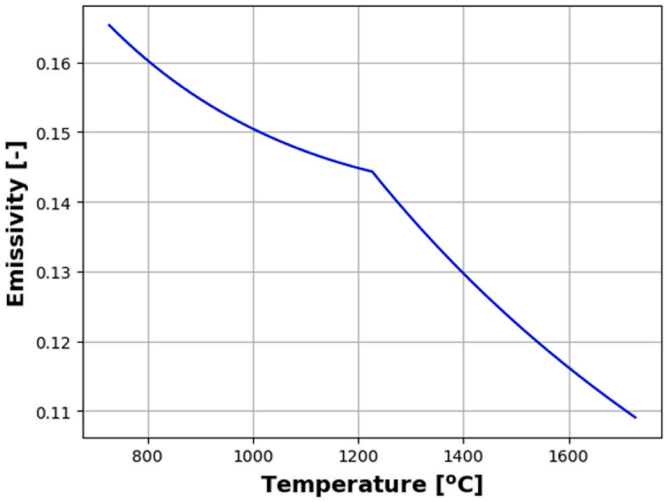

Fig. C-2. CO_2 emissivity as a function of temperature.

Appendix D. Estimation of convective heat loss coefficient parameters

Assuming that the heat loss from the outer drum to the environment is due to external free convection from a long horizontal cylinder, the Nusselt number (Nu_D) is given by equation D-1 [16].

$$Nu_D = \left(0.6 + \frac{0.387(Ra_D)^{1/6}}{\left[1 + (0.559/Pr)^{9/16}\right]^{8/27}}\right)^2 \tag{D-1}$$

In equation D-1, Ra_D is the Rayleigh number and Pr is the Prandtl number, which are given by equations D-2 and D-3.

$$Ra_D = \frac{g\beta\left(T_{d,o} - T_a\right)\left(d_{d,o}\right)^3}{\vartheta_a \alpha_a} \tag{D-2}$$

$$Pr = \frac{c_{p,a}\mu_a}{k_a} \tag{D-3}$$

In equations D-2 and D-3, β is the thermal expansion coefficient [1/K] (given by equation D-4 by assuming air as an ideal gas), T_f is the average temperature between outer wall and ambient air [K], ϑ_a is the kinematic viscosity of the air [m^2/s] (Equation D-5), α_a is the thermal diffusivity of air [m^2/s] (Equation D-6), ρ_a is the density of air [kg/m^3] (Equation D-7), k_a is the thermal conductivity of air [W/(m·K)] (Equation D-8 [36]), $c_{p,a}$ is the specific heat of the air [J/(kg·K)] (Equation D-9 [36]) and μ_a is the dynamic viscosity of the air [Pa·s] (Equation D-10 [36]).

$$\beta = \frac{1}{T_f} \tag{D-4}$$

$$\vartheta_a = \frac{\mu_a}{\rho_a} \tag{D-5}$$

$$\alpha_a = \frac{k_a}{\rho_a c_{p,a}} \tag{D-6}$$

$$\rho_a = \frac{p_a M_a}{R T_f} \tag{D-7}$$

$$k_a = \frac{0.00031417 \times T_f^{0.7786}}{1 - \frac{0.7116}{T_f} + \frac{2121.7}{T_f^2}} \tag{D-8}$$

$$c_{p,a} = \left(28958 + 9390\left(\frac{3012/T_f}{\sinh(3012/T_f)}\right)^2 + 7580\left(\frac{1484/T_f}{\cosh(1484/T_f)}\right)^2\right)\frac{1}{M_a} \tag{D-9}$$

$$\mu_a = \frac{1.43 \times 10^{-6} \times T_f^{0.5039}}{1 + \frac{108.3}{T_f}} \tag{D-10}$$

References

[1] IEA, Renewables, 2020. https://www.iea.org/reports/renewables-2020. (Accessed 21 November 2022). accessed.
[2] M. Stork, W. Meindertsma, M. Overgaag, M. Neelis, Technical Report: A Competitive and Efficient Lime Industry, EuLA, 2014.
[3] R.M. Jacob, L.A. Tokheim, Electrified calciner concept for CO2 capture in pyro-processing of a dry process cement plant, Energy 268 (2023), 126673, https://doi.org/10.1016/j.energy.2023.126673.
[4] M. Simoni, M.D. Wilkes, S. Brown, J.L. Provis, H. Kinoshita, Decarbonising the lime industry: state-of-the-art, Renew. Sustain. Energy Rev. 168 (2022), 112765, https://doi.org/10.1016/j.rser.2022.112765.
[5] H. Piringer, Lime shaft kilns, Energy Proc. 120 (2017) 75–95, https://doi.org/10.1016/j.egypro.2017.07.156.
[6] T.P. Hills, M. Sceats, D. Rennie, P. Fennell, LEILAC: low cost CO2 capture for the cement and lime industries, Energy Proc. 114 (2017) 6166–6170, https://doi.org/10.1016/j.egypro.2017.03.1753.
[7] CORDIS, Low Emissions Intensity Lime and Cement 2: Demonstration Scale, 2021. https://cordis.europa.eu/project/id/884170. accessed 23.01.23.
[8] O. Katajisto, Calcination of Calcium Carbonate Based Materials in Electric Heated Rotary Kiln, Master's thesis, Tampere University, 2020.
[9] T. Suzuki, T. Okazaki, K. Yamamoto, H. Nakata, O. Fujita, Improvements in pyrolysis of wastes in an externally heated rotary kiln, J. Therm. Sci. Technol. 3 (2008) 532–539, https://doi.org/10.1299/jtst.3.532.
[10] W.D.G. Estrada, R. Albuja, I.B. Dávila, B.S. Rueda, L. Corredor, A.G. Quiroga, H. Maury, Transient operation effects on the thermal and mechanical response of a large-scale rotary kiln, Result Eng. 14 (2022), 100396, https://doi.org/10.1016/j.rineng.2022.100396.
[11] M. Sheikholeslami, Numerical investigation of solar system equipped with innovative turbulator and hybrid nanofluid, Sol. Energy Mater. Sol. Cell. 243 (2022), 111786, https://doi.org/10.1016/j.solmat.2022.111786.
[12] C. Zhai, M.D. Islam, R. Simmons, I. Barsoum, Heat transfer augmentation in a circular tube with delta winglet vortex generator pairs, Int. J. Therm. Sci. 140 (2019) 480–490, https://doi.org/10.1016/j.ijthermalsci.2019.03.020.
[13] V.R. Sharma, S. Sankalp, N. Madhwesh, M.S. Manjunath, Enhanced thermal performance of tubular heat exchanger using triangular wing vortex generator, Cogent Eng. 9 (2022), 2050021, https://doi.org/10.1080/23311916.2022.2050021.
[14] N. Jayranaiwachira, P. Promvonge, C. Thianpong, S. Skullong, Entropy generation and thermal performance of tubular heat exchanger fitted with louvered corner-curved V-baffles, Int. J. Heat Mass Tran. 201 (2023), 123638, https://doi.org/10.1016/j.ijheatmasstransfer.2022.123638.
[15] G. Moumin, S. Tescari, C. Sattler, Impact of bed motion on the wall-to-bed heat transfer for powders in a rotary kiln and effect of built-ins, Int. J. Heat Mass Tran. 177 (2021), https://doi.org/10.1016/j.ijheatmasstransfer.2021.121473.
[16] F.P. Incropera, D.P. Dewitt, T.L. Bergman, A.S. Lavine, Principles of Heat and Mass Transfer, eighth ed., John Wiley & Sons, Singapore, 2017.
[17] V.K. Nangia, N.S. Grewal, B.S. Rao, Normal total emittance of limestone, Int. Commun. Heat Mass Tran. 15 (1988) 681–687, https://doi.org/10.1016/0735-1933(88)90058-9.
[18] C.N. Satterfield, F. Feakes, Kinetics of the thermal decomposition of calcium carbonate, AIChE J. 5 (1959) 115–122, https://doi.org/10.1002/aic.690050124.
[19] R.H. Borgwardt, Calcination kinetics and surface area of dispersed limestone particles, AIChE J. 31 (1985) 103–111, https://doi.org/10.1002/aic.690310112.
[20] T.B. Drenhaus, E. Simsek, S. Wirtz, V. Scherer, A coupled fluid dynamic-discrete element simulation of heat and mass transfer in a lime shaft kiln, Chem. Eng. Sci. 65 (2010) 2821–2834, https://doi.org/10.1016/j.ces.2010.01.015.
[21] G.D. Silcox, J.C. Kramlich, D.W. Pershing, A mathematical model for the flash calcination of dispersed calcium carbonate and calcium hydroxide particles, Ind. Eng. Chem. Res. 28 (1989) 155–160, https://doi.org/10.1021/ie00086a005.
[22] H. Mikulčić, E.V. Berg, M. Vujanović, P. Priesching, L. Perković, R. Tatschl, N. Duić, Numerical modelling of calcination reaction mechanism for cement production, Chem. Eng. Sci. 69 (2012) 607–615, https://doi.org/10.1016/j.ces.2011.11.024.
[23] F.R. Campbell, A.W.D. Hills, Transport properties of porous lime and their influence on the decomposition of porous compacts of calcium carbonate, Chem. Eng. Sci. 25 (1970) 929–942, https://doi.org/10.1016/0009-2509(70)85038-2.
[24] B.R. Stanmore, P. Gilot, Review - calcination and carbonation of limestone during thermal cycling for CO2 sequestration, Fuel Process. Technol. 86 (2005) 1707–1743, https://doi.org/10.1016/j.fuproc.2005.01.023.
[25] W.L. McCabe, J.C. Smith, P. Harriott, Unit Operations of Chemical Engineering, seventh ed., McGraw-Hill, 2005.
[26] C.J. Geankoplis, Transport Processes and Unit Operations, third ed., Prentice-Hall Internation, 1993.
[27] M. Orfeuil, Electric Process Heating: Technologies/Equipment/Applications, Battelle Press, 1987.
[28] S.H. Tscheng, A.P. Watkinson, Convective heat transfer in a rotary kiln, Can. J. Chem. Eng. 57 (1979) 433–443, https://doi.org/10.1002/cjce.5450570405.
[29] D. Kunii, J.M. Smith, Heat transfer characteristics of porous rocks, AIChE J. 6 (1960) 71–77, https://doi.org/10.1002/aic.690060115.
[30] S. Lupi, Fundamentals of Electroheat: Electrical Technologies for Process Heating, Springer, 2017.
[31] Kanthal, Silicon carbide heating elements (Globar® SD). https://www.kanthal.com/en/products/furnace-products/electric-heating-elements/silicon-carbide-heating-elements/#tab-downloads. (Accessed 14 February 2023) accessed.
[32] Statistics Norway, Electricity prices. https://www.ssb.no/en/energi-og-industri/energi/statistikk/elektrisitetspriser. (Accessed 14 February 2023) accessed.
[33] D. Kunii, T. Chisaki, Rotary Reactor Engineering, Elsevier, Amsterdam, 2008.
[34] I. Barin, Thermochemical Data of Pure Substances, VCH Publishers, 1995.
[35] J.R. Howell, A catalog of radiation heat transfer configuration factors. http://www.thermalradiation.net/indexCat.html. (Accessed 21 November 2022) accessed.
[36] D.W. Green, R.H. Perry, Perry's Chemical Engineering Handbook, McGraw-Hill, 2008.